

Self-appearance-aided Differential Evolution for Motion Transfer

Peirong Liu¹ Rui Wang² Xuefei Cao² Yipin Zhou² Ashish Shah²
 Maxime Oquab² Camille Couprie² Ser-Nam Lim²

¹University of North Carolina at Chapel Hill ²Facebook AI

peirong@cs.unc.edu

{raywang, xuefeicao01, yipinzhou, ashishbshah, gas, couprie, sernamlim}@fb.com

Abstract

Image animation transfers the motion of a driving video to a static object in a source image, while keeping the source identity unchanged (Fig. 1). Great progress has been made in unsupervised motion transfer recently, where no labelled data or ground truth domain priors are needed. However, current unsupervised approaches still struggle when there are large motion or viewpoint discrepancies between the source and driving images. In this paper, we introduce three measures that we found to be effective for overcoming such large viewpoint changes. Firstly, to achieve more fine-grained motion deformation fields, we propose to apply Neural-ODEs for parametrizing the evolution dynamics of the motion transfer from source to driving. Secondly, to handle occlusions caused by large viewpoint and motion changes, we take advantage of the appearance flow obtained from the source image itself (“self-appearance”), which essentially “borrows” similar structures from other regions of an image to inpaint missing regions. Finally, our framework is also able to leverage the information from additional reference views which help to drive the source identity in spite of varying motion state. Extensive experiments demonstrate that our approach outperforms the state-of-the-arts by a significant margin ($\approx 40\%$), across six benchmarks varying from human faces, human bodies to robots and cartoon characters. Model generality analysis indicates that our approach generalises the best across different object categories as well.¹

1. Introduction

Motion transfer (or image animation) animates a source object according to the motion derived from a driving video, where the object identities in the source and driving images could be different (Fig. 1). It has a wide range of

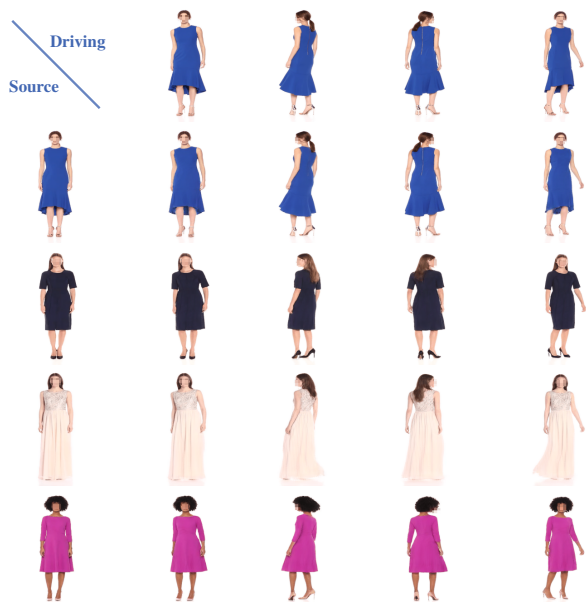


Figure 1. Motion transfer on Fashion. The source and driving images could contain the same or different identities. In either scenario, the source object is expected to derive its motion from that of the driving video, while preserving its original identity.

applications including in the field of education and entertainment, and has been used recently in video conferencing [28, 44, 49]. Traditional motion transfer approaches typically require a large amount of labelled data such as manually-selected landmarks, semantics segmentations, parametric 3D models [2, 4, 31, 39, 50, 55]. More recent deep generative models such as GAN/VAE-based works avoid the need of object modelling but still depend on pre-trained object-specific representation models such as keypoints, poses and shapes extractors [5, 6, 13, 32, 43].

Most recently, a stream of unsupervised motion transfer approaches have been proposed to avoid relying on specific domain priors or significant labeling efforts. Most of them

¹Our code will be publicly available.

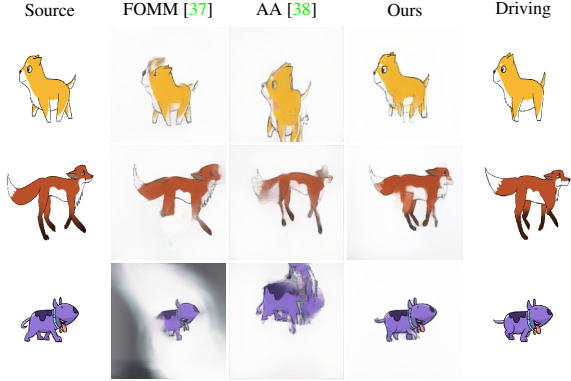


Figure 2. Comparison results for model generality on MGif. Images are generated by models trained on VoxCeleb dataset.

leverage unsupervised key-points [36, 37, 44, 46] or regions [38] extractors for approximating the motion deformation field between the source and driving domains. An encoder-decoder network is then used to extract features from the source image, which are then warped to the driving domain according to the predicted deformation during generation. These unsupervised approaches could be trained end-to-end without additional domain priors, which makes it possible to animate a broader range of objects.

However, without pre-specific models (e.g., 3D morphable models [2]) or domain priors (e.g., extracted poses [32, 43]) of the source object as additional inputs, it is particularly challenging for the above unsupervised approaches to animate a source object on most scenarios with relatively large driving motion changes. (1) the key-point/region-based motion transformation could only deform the source image to a small portion of the target domain, while a large portion under the driving view still remains unknown; (2) without additional viewpoint/domain information, all the missing regions under the driving view needs to be inpainted by the image generator (decoder) from scratch, which tends to produce visually unrealistic results (Fig. 2).

To overcome the above-mentioned issues, we propose an end-to-end framework for unsupervised motion transfer that comprises three major components:

- *Differentially-refined motion transfer.* Our framework adopts neural-ODEs for modeling the evolution dynamics of motion deformation field from source to driving domain, which could be viewed as a differentiable refinement of the initially sparse key-points displacements. This helps to avoid expensive flow computations (e.g., Jacobians in [36, 44], singular value decompositions (SVD) in [38]), while achieving comparable performance.
- *Self-appearance-aided inpainting.* To handle occlusions in the driving views, our framework utilizes an

appearance flow vector field to inpaint missing regions in the resulting frames with similar structures from the source image.

- *Driving-view feature fusion.* Our framework further learns to fuse the features from additional source reference views when transferring to the driving domain.

Experiments across six datasets containing human faces, human bodies, robots, and cartoon animals consistently demonstrate that our approach outperforms the state-of-the-arts by a significant margin ($\approx 40\%$). Further discussions on model generality show that our approach generalises better and performs the most stable when tested across different object categories.

2. Related Work

Image Animation Image animation transfers the motion information from one driving video to a source image, where the identities in the source image and driving video are not necessarily the same. Traditional supervised approaches require pre-specified landmarks, segmentations or 3D models and are typically limited to specific domains (e.g., face, bodies, etc) [2, 4, 13, 31, 39, 50, 55]. These approaches usually require a large amount of labelled data, making them hard to scale to a wider range of animation objects [36, 38]. Recently, several unsupervised approaches have been proposed to address the above challenges [36–38, 42, 44, 46, 49]. For instance, the MonkeyNet [36] learns a set of key-points for sparse motions prediction in an unsupervised manner, while the first order motion model (FOMM) [37] further improves it by additionally considering a local affine transformation to generate animations. The articulated-animation model (AA) [38] on the other hand approximates the motion deformation via a principal component analysis (PCA) on the heatmaps of the learned sparse motions. By leveraging unsupervised approaches, researchers have been able to scale image animation to a wider range of objects, e.g., faces, bodies, robots, and cartoon animals [36, 37].

Few-Shot Motion Retargeting For better generalization to unseen domains and large motion changes, models were proposed to take more than one image of the source object with arbitrary poses at reference time. This few-shot strategy has been recently used in face reenactment [15, 31, 50], body retargeting [19, 20, 22, 23, 32, 42], clothing transfer [1, 25, 26, 30], etc. However, all these works rely on specific object representations such as 3D meshes, facial landmarks or body poses as conditional inputs, which need to be pre-specified by pre-trained models. This limits the few-shot retargeting settings for a broader applications on objects where representations are not well-explored. Our ap-

proach, on the other hand, does not need any additional pre-defined object representation. With only a few images of the source object and a driving video, our proposed framework learns to extract, warp features from all input images solely according to the driving motion, and then leverage the individual strength of all features under the driving domain, in an entirely unsupervised way. This makes it possible for applying the few-shot motion transfer setting on a broader range of objects in addition to faces/bodies, such as robots and cartoon characters experimented in this paper (Sec. 4).

Neural-ODEs Ordinary differential equations (ODEs) are widely used to represent the evolution of system dynamics. Models such as residual networks and recurrent neural networks, represent complex transformations by predicting a sequence of changes as the hidden states [24, 34]. Chen et al. [7] proposed neural-ODEs to parameterize the continuous dynamics of hidden units using a deep-network-specified ODE. They were able to keep the training memory unchanged via the adjoint sensitivity method that avoids memory explosion resulting from backpropagating through continuous-depth networks. AN-ODE [52] addressed the instability issue of neural-ODEs by Discretize-Then-Optimize (DTO) differentiation. Going beyond the transport phenomena in physics and chemistry, neural-ODEs have been recently used in computer vision applications, such as image segmentation [41], reconstruction [47], super-resolution [29], classification [16], and perfusion imaging [21], where neural-ODEs are proven to be better capable of capturing complex transformations via the continuous evolution of the system dynamics. In this work, we employ neural-ODEs to differentially refine a pixel-wise dense motion transformation between the source and driving images, which evolved from the sparse (coarse) motion fields represented by key-points displacements. The benefit of utilizing differential motion evolution lies in the generalization of sparse-to-dense motion prediction, while avoiding computationally expensive Jacobians or SVD operations [37, 38, 44].

Appearance Flow Appearance flow proposed by Zhou et al. [54] was originally designed to generate target views from source views via a flow-based approach by learning to predict a 2D vector field, i.e., the appearance flow field, which warps the source domain to the target domain based on similarity in appearance. This idea has been widely applied in the field of computer vision. For instance, Godard et al. [14] utilized appearance matching for depth estimation. Ren et al. [33] introduced appearance flow for image inpainting tasks, where it is used to predict the offset vectors that specify which pixels in the source view should be moved to reconstruct the target view for inpainting the missing regions. We adapt the appearance flow in our proposed

framework to deform the appearance from regions of the source image to the occluded regions after motion transformation. Doing so helps to enhance the inpainting capability of the image generation network in our framework as demonstrated in our experimental results (Fig. 6, Tab. 3).

3. Method

Let $\mathbb{S} = \mathbb{S}(\mathbf{x})$ ($\mathbf{x} \in \Omega$) denotes a source image containing the source object, and $\mathbb{D} \in \{\mathbb{D}(\mathbf{x}, i) | \mathbf{x} \in \Omega, i = 0, 1, \dots, T\}$ refers to the set of images in a driving video. In this paper, we aim to generate a series of images $\mathbb{S}_{\mathbb{D}} \in \{\mathbb{S}_{\mathbb{D}}(\mathbf{x}, i) | \mathbf{x} \in \Omega, i = 0, 1, \dots, T\}$ from \mathbb{S} , where each generated image preserves the same object identity as \mathbb{S} while borrowing the motions from \mathbb{D} . When \mathbb{S} and \mathbb{D} contain the same identity, the generation reduces to a video reconstruction task. In the case of \mathbb{S} and \mathbb{D} containing different identities, the generation is a general motion transfer task. Our proposed approach can be applied to both scenarios.

In general, our framework (Fig. 3) consists of three major components: (1) Motion evolution, which predicts a dense deformation field differentially refined from initially sparse motions between \mathbb{S} and \mathbb{D} ; (2) Self-appearance-aided image generation, which inpaints the missing regions of \mathbb{S} under the driving motion, with the help of self-appearance deformation field predicted from \mathbb{S} itself; (3) Driving-view feature fusion, which leverages the predictions from the source and multiple reference images that cover different domains of the source object for the final prediction of $\mathbb{S}_{\mathbb{D}}$ on the driving domain.

3.1. Motion Evolution with Neural-ODE

In this section, we aim to predict a pixel-wise motion deformation field $\mathcal{T}_{\mathbb{S} \rightarrow \mathbb{D}}$ between \mathbb{S} and \mathbb{D} . Our approach consists of two steps: (1) Keypoints-based coarse motion prediction; (2) Neural-ODE-based dense motion evolution. We first obtain K keypoints for both \mathbb{S} and \mathbb{D} :

$$\mathbf{x}_{\mathbb{S}}^i = \mathcal{F}_K(\mathbb{S}), \mathbf{x}_{\mathbb{D}}^i = \mathcal{F}_K(\mathbb{D}), \quad i = 1, \dots, K, \quad (1)$$

where \mathcal{F}_K is an encoder-decoder network for self-supervised keypoints detection [36, 37, 44]. The keypoint-wise displacements between \mathbb{S} and \mathbb{D} are therefore:

$$\{\Delta^0, \Delta^i = \mathbf{x}_{\mathbb{S}}^i - \mathbf{x}_{\mathbb{D}}^i | i = 1, \dots, K\}, \quad (2)$$

where $\Delta^0 := \mathbf{0}$ represents an additional keypoint displacement for the static background.

The $K + 1$ local displacements $\{\Delta^i\}$ are then forwarded into a convolutional network \mathcal{F}_C which outputs the corresponding coefficient maps $\{\alpha^i\}$ for regressing all the sparse keypoint-wise displacements:

$$\widetilde{\mathcal{T}} = \sum_{i=0}^K \alpha^i \Delta^i, \quad i = 0, 1, \dots, K. \quad (3)$$

$\widetilde{\mathcal{T}}$ acts as a coarse prediction for the motion trajectories between \mathbb{S} and \mathbb{D} .

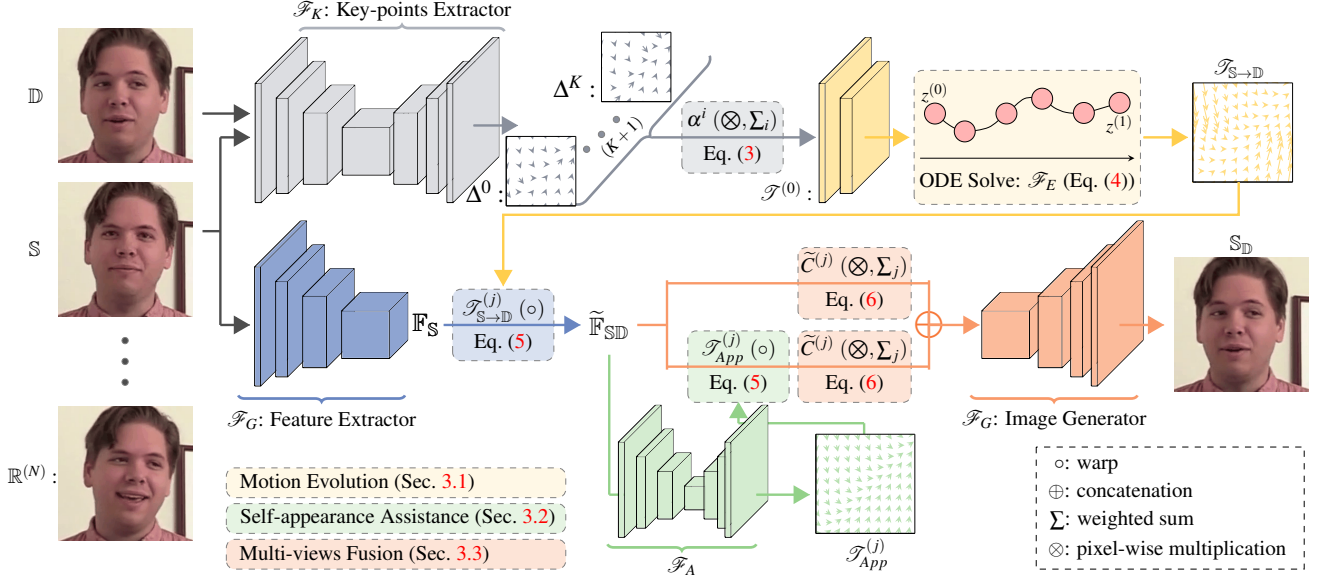


Figure 3. Framework bird’s eye view. The driving, source and reference images first go through a key-point extractor to obtain the initial sparse motions between driving and each of the source and reference images. The sparse motions are then further refined to a dense motion deformation field via neural-ODEs (Sec. 3.1). Based on the predicted dense motion fields, the features extracted from source and reference images are warped to the driving domain correspondingly. The weighted-sum features are obtained by leveraging between all warped features along with their self-appearance-aided features under the driving domain (Sec. 3.2-3.3). A decoder then outputs the final prediction of the generated image.

We propose to solve the resulting pixel-wise motion deformation $\mathcal{T}_{S \rightarrow D}$ in a general form as an initial value problem [7]. Specifically, we consider the regressed deformation $\tilde{\mathcal{T}}$ as the initial state $\mathcal{T}^{(0)}$ for the differential equation:

$$\frac{d\mathcal{T}}{dt} = \mathcal{F}_E(\mathcal{T}^{(t)}, t), \quad \text{for } t \in [0, 1], \quad (4)$$

where \mathcal{F}_E is a convolutional network estimating the motion evolution dynamics [7]. Essentially, the integration of Eq. (4) leads $\mathcal{T}^{(0)}$ to the final result of the refined motion deformation $\mathcal{T}^{(1)}$. We employ the adjoint back-propagation by Chen et al. [7, 41, 52] to reduce memory consumption.

In Monkey-Net [36], the regression output $\tilde{\mathcal{T}}$ is directly used to warp the source image \mathbb{S} which then fed into an image generator for final prediction. In FOMM [37], additional first-order displacements are used for predicting the regression coefficients. In [38], the sparse displacements are alternatively formulated via principal component analysis (PCA). Our motion evolution approach is a generalized model applicable for all the above approaches. Without motion evolution in Eq. (4), our framework could be reduced to [36–38], where the initial status $\mathcal{T}^{(0)}$ formulated in the corresponding work is directly used as $\mathcal{T}_{S \rightarrow D}$ prediction.

3.2. Self-appearance-aided Generation

After predicting the dense motion deformation $\mathcal{T}_{S \rightarrow D}$, an encoder-decoder-structured generator \mathcal{F}_G is used to obtain

the prediction of \mathbb{S}_D [36, 37, 44]. In short, it first extracts features (\mathbb{F}_S) from the input source image \mathbb{S} , and warps the source features \mathbb{F}_S to the driving domain via $\mathcal{T}_{S \rightarrow D}$ to produce the set of warped features, \mathbb{F}_{SD} , in a pixel-wise manner. \mathcal{F}_G then decodes \mathbb{F}_{SD} and inpaints the missing regions under the driving viewpoint to generate the final prediction.

In reality, large deformation resulting from pose and expression changes are common, e.g., head turning right from left, eyes opening and closing, and we find that \mathcal{F}_G tends to struggle to inpaint most missing regions (Fig. ??, 4). For instance, it is challenging for \mathcal{F}_G to infer the realistic details of the left side of one’s face if only the right side is visible in the source image. To overcome this, we adopt the appearance flow, which was originally proposed by [54] to generate target scenes (objects) from source scenes (objects) using a flow-based method, but has also been utilized for image inpainting tasks [33]. For image neighborhoods with symmetrical structures, especially in the case of human heads or bodies, features in the existing regions of the source domain itself can be effectively re-used by appearance flow to assist \mathcal{F}_G in generating textures for missing regions after the motion deformation. We describe such a procedure as self-appearance assistance.

Specifically, to more realistically inpaint missing regions, we apply an encoder-decoder network \mathcal{F}_A to predict the self-appearance flow deformation field \mathcal{T}_{App} which is used to warp (“flow”) features from their original regions to

the missing regions:

$$\mathbb{F}_{App} = \mathcal{T}_{App} \circ \tilde{\mathbb{F}}_{SD}, \quad \tilde{\mathbb{F}}_{SD} = \mathcal{T}_{S \rightarrow D} \circ \mathbb{F}_S. \quad (5)$$

The self-appearance-warped source features \mathbb{F}_{App} and the dense-motion-warped source features $\tilde{\mathbb{F}}_{SD}$ are then concatenated and fed into the decoder part of \mathcal{F}_G for image generation (Fig. 3). In this way, \mathcal{F}_A learns when and where to copy from the source image to the missing regions (if similar parts exists), thus reducing the burden on \mathcal{F}_G to generate all the missing regions from scratch.

3.3. Leveraging Multiple Input Views

While self-appearance assistance is capable of enhancing image generation in the driving domain, information from only a single view of the source object remains a limiting factor. For instance, inferring the details of an object's back view would be challenging if \mathcal{F}_G is only given a source image with front view. Therefore, we further enable the generation module \mathcal{F}_G to fuse the warped features under the driving domain from multiple (N) reference views ($\{\mathbb{R}^{(j)}\}_N$) along with those from the source image (\mathbb{S}).

Specifically, the generator \mathcal{F}_G additionally outputs a soft confidence mask $C^{(j)} (j = 0, \dots, N, C^{(0)} \text{ for } \mathbb{S})$ that indicates the per-pixel prediction quality of each input view $\mathbb{S}, \{\mathbb{R}^{(j)}\}_N$ — this is implemented by simply adding an additional output layer to the last decoder layer of \mathcal{F}_C . The confidence masks for all input views are further normalized to sum to one at each pixel location: $\tilde{C}^{(j)}(\mathbf{x}) = C^{(j)}(\mathbf{x}) / \sum_{j=0}^N C^{(j)}(\mathbf{x})$. The weighted-sum of the dense-motion-warped features and the appearance-warped features are then given as:

$$\tilde{\mathbb{F}}_{App} = \sum_{j=1}^N \tilde{C}^{(j)} \mathbb{F}_{App}^{(j)}, \quad \tilde{\mathbb{F}}_{D} = \sum_{j=1}^N \tilde{C}^{(j)} \tilde{\mathbb{F}}^{(j)} \quad (6)$$

Similar to Sec. 3.2, the weighted-summed self-appearance-warped features ($\tilde{\mathbb{F}}_{App}$) and the motion-transformation-warped features ($\tilde{\mathbb{F}}_{SD}$) are then concatenated and fed into \mathcal{F}_G for the final prediction of \mathbb{S}_D .

3.4. Losses

Following prior work [37, 38], we compute the multi-resolution perceptual reconstruction loss between the generated \mathbb{S}_D and driving frame \mathbb{D} , in the feature space generated with pre-trained VGG-19 [18] network:

$$\mathcal{L}_{\text{percep}}(\mathbb{S}_D, \mathbb{D}) = \sum_{i=1}^5 \sum_{j=1}^4 |V_i(\mathbb{S}_D, j) - V_i(\mathbb{D}_j)|, \quad (7)$$

where i denotes the i^{th} layer of the VGG-19, and j refers to the j^{th} downsampling level of corresponding images.

Equivariance loss [17, 37] is also imposed to encourage consistency in the set of keypoints being extracted under different geometric transformations:

$$\mathcal{L}_{\text{equiv}} = |\mathcal{T} \circ \mathcal{F}_K(\mathbb{I}) - \mathcal{F}_K(\mathcal{T} \circ \mathbb{I})|, \quad (8)$$

where \mathbb{I} refers to an image to be transformed, \mathcal{T} denotes a known transformation operator, and \mathcal{F}_K is the keypoint extractor. Overall, the framework is trained end-to-end with the sum-up loss:

$$\mathcal{L} = \mathcal{L}_{\text{percep}} + \lambda \mathcal{L}_{\text{equiv}}, \quad \lambda > 0. \quad (9)$$

4. Experiments

We evaluate the performance of our proposed framework on three tasks: (1) Video reconstruction, where the source image and driving video contains the same object identity; (2) Motion transfer, where the source image and driving video hold different identities; (3) Model generality, where we test the models on externally extracted videos which are outside the scope of their training datasets. This section starts with datasets and metrics description, followed by comparisons with the current state of art works, and model ablation studies. We compare our model with three current state-of-the-art methods: FOMM [37], Articulated Animation [38] and face-vid2vid [44]. Extensive experiments consistently show that our model significantly outperforms the state-of-the-arts across different datasets with objects varying from human faces, human bodies to robots and cartoons, and is well-generalized to a wide range of out-of-scope datasets as well.

Datasets We experimented on eight datasets below.

- **VoxCeleb** [27]: a talking head video dataset extracted from YouTube. We used the same pre-processing and train-test splitting strategies with [37], where all video frames were cropped according to the bounding boxes for face-tracking. We obtained 18,314 videos for training and 507 for testing, with lengths varying from 64 to 1,024 frames. All videos were resized to 256×256 preserving the aspect ratio.
- **DFDC** [11]: the Deepfake Detection Challenge dataset, from which we collected all 16,846 real videos (15,039 videos for training and 1,807 for testing), each with 300 frames. The videos were pre-processed to contain only the talking-heads following the same pipeline with VoxCeleb.
- **UvA-Nemo** [9, 10]: a facial analysis dataset containing 1,234 videos, each of which starts with a neutral expression. Following [37, 45], we used 1,110 videos for training and 124 for testing.
- **AIST Dance DB** [40]: a large-scale dance dataset containing 12,670 original dance videos (12,187 for training, 493 for testing) including various dance genres, with lengths varying from 400 to 1,800 frames. All videos were cropped according to body tracking² and resized to 256×256 preserving the aspect ratio.

²Code in <https://github.com/ITCoders/Human-detection-and-Tracking>

Dataset	Method	Video Reconstruction						Image Animation	
		L1 (↓)	LPIPS (↓)	FID (↓)	MS-/SSIM (↑)	PSNR (↑)	AKD (↓)	FID (↓)	CSIM (↑)
VoxCeleb (507)	FOMM [37]	0.047 (0.040)	0.14 (0.11)	50.96 (43.28)	0.84/0.75 (0.87/0.78)	22.74 (23.77)	2.29 (1.36)	62.88 (52.10)	0.78 (0.81)
	AA [38]	0.044 (0.034)	0.13 (0.18)	50.69 (44.02)	0.86/0.77 (0.90/0.82)	23.18 (24.61)	2.15 (1.26)	86.03 (79.59)	0.75 (0.75)
	f-v2v [44]	0.042	N/A	69.13	0.85/0.80	24.37	2.07	55.64	0.75
	Ours	0.027	0.070	25.43	0.93/0.86	26.20	1.18	47.21	0.90
DFDC (1807)	FOMM [37]	0.034 (0.029)	0.140 (0.119)	61.59 (51.59)	0.86/0.80 (0.89/0.82)	25.65 (26.72)	2.81 (2.42)	84.18 (78.76)	0.81 (0.85)
	AA [38]	0.039 (0.035)	0.156 (0.140)	89.88 (83.79)	0.86/0.79 (0.89/0.80)	23.64 (24.21)	2.52 (2.43)	172.35 (156.32)	0.73 (0.74)
	Ours	0.018	0.0061	33.22	0.95/0.91	27.99	1.28	64.89	0.92
Nemo (124)	FOMM [37]	0.0139 (0.0120)	0.034 (0.027)	19.60 (18.03)	0.96/0.95 (0.97/0.95)	32.90 (33.91)	1.17 (1.12)	27.46 (23.80)	0.93 (0.94)
	AA [38]	0.0169 (0.0151)	0.041 (0.037)	30.09 (40.31)	0.95/0.93 (0.96/0.94)	30.55 (31.00)	1.32 (1.24)	72.11 (67.65)	0.83 (0.83)
	Ours	0.0061	0.013	10.35	0.99/0.98	39.40	0.87	23.46	0.98
Fashion (100)	FOMM [37]	0.013 (0.013)	0.033 (0.033)	30.73 (30.18)	0.96/0.93 (0.95/0.93)	27.06 (26.12)	1.09 (1.08)	41.10 (39.52)	0.99 (0.99)
	AA [38]	0.015 (0.014)	0.040 (0.039)	37.99 (36.10)	0.95/0.92 (0.96/0.92)	25.88 (25.98)	1.54 (1.50)	78.01 (70.76)	0.99 (0.99)
	Ours	0.010	0.030	22.25	0.97/0.95	26.95	1.00	32.64	0.99
AIST (493)	FOMM [37]	0.015 (0.013)	0.056 (0.048)	63.17 (49.33)	0.94/0.94 (0.95/0.94)	26.27 (26.92)	6.69 (5.47)	114.57 (109.81)	0.99 (0.99)
	AA [38]	0.029 (0.028)	0.239 (0.234)	99.95 (91.93)	0.94/0.91 (0.95/0.92)	20.40 (20.54)	5.67 (5.09)	198.43 (182.63)	0.98 (0.99)
	Ours	0.011	0.043	37.71	0.96/0.95	26.97	3.66	105.20	0.99
Tai-Chi-HD (87)	FOMM [37]	0.057 (0.046)	0.24 (0.18)	123.78 (95.95)	0.69/0.64 (0.77/0.72)	20.45 (21.73)	9.69 (7.87)	148.86 (134.46)	0.99 (0.99)
	AA [38]	0.059 (0.053)	0.21 (0.17)	109.56 (86.57)	0.70/0.57 (0.76/0.63)	20.31 (21.19)	7.30 (6.67)	159.54 (147.73)	0.99 (0.99)
	Ours	0.035	0.15	76.41	0.83/0.78	23.08	6.36	123.10	0.99
Bair (128)	FOMM [37]	0.030 (0.024)	0.067 (0.047)	107.70 (45.41)	0.91/0.88 (0.94/0.91)	23.64 (25.35)	N/A	107.70 (114.54)	N/A
	AA [38]	0.052 (0.048)	0.137 (0.121)	217.87 (77.14)	0.87/0.76 (0.90/0.77)	19.75 (19.75)	N/A	217.87 (201.78)	N/A
	Ours	0.018	0.027	34.44	(0.97) 0.94	27.75	N/A	96.91	N/A
MGif (100)	FOMM [37]	0.033 (0.031)	0.112 (0.106)	154.88 (146.46)	0.87/0.84 (0.87/0.84)	19.56 (19.79)	N/A	196.94 (183.68)	N/A
	AA [38]	0.026 (0.026)	0.092 (0.089)	136.84 (131.89)	0.90/0.85 (0.90/0.86)	20.22 (20.35)	N/A	331.72 (315.71)	N/A
	Ours	0.021	0.072	117.74	(0.92) 0.90	21.34	N/A	180.30	N/A

Table 1. Comparing FOMM [37], Articulated Animation (AA) [38], face-vid2vid (f-v2v) [44] (reported) and our approach on human face datasets (VoxCeleb, DFDC, Nemo), human body datasets (Fashion, AIST, Tai-Chi-HD), robot dataset (Bair) and cartoon animal dataset (MGif). The number of reconstruction testing samples are listed in parentheses below each dataset name. For animation tests, 200 source-driving object pairs are randomly generated for each dataset. Results are reported in mean format with best ones bolded. ↓ (↑) denotes that lower (higher) is better. For one-shot baseline models, we additionally list, in the parentheses, the best scores (L1 for reconstruction, FID for animation) computed from the same reference images used in our model. Our approach consistently achieves the best performance on *all* metrics across *all* eight datasets.

- Tai-Chi-HD [27]: a dataset containing 769 tai-chi videos from YouTube following [27]. Overall, 682 videos were used for training and 87 for testing.
- Fashion [48]: a dataset containing 600 videos (500 for training, 100 for testing), each with around 350 frames. Each video consists of a model testing clothes with diverse appearances and textures.
- BAIR [12]: a robot pushing dataset containing 43,008 videos (42,880 for training, 128 for testing) collected by a Sawyer robotic arm pushing diverse objects. Each video has 30 frames with 256×256 resolution.
- MGif [36]: a dataset containing 1,000 videos (900 for training, 100 for testing) of different moving 2D cartoon animals, with each video as a gif file.

Metrics We list below the metrics we used for evaluating different individual tasks.

- Reconstruction correctness (for video reconstruction):

- L1: the average L1 distance between the generated and real images, which indicates the overall reconstruction correctness.
- LPIPS [51]: the perceptual distance between the generated and real images, which correlates better with human observations compared to L1.
- PSNR: the mean squared error (MSE) between the generated and real images which measures the reconstruction quality.
- MS-/SSIM: SSIM measures the structural similarity between the generated and real images which is a more robust indicator than PSNR [44]. MS-SSIM is a multi-scale variant of SSIM working on multiple scales of the images and has been shown to correlate well with human perception.

- Video quality – FID (Fréchet Inception Distance): measures the distance between the distributions of the generated and real images. We use PyTorch’s official implementation [35], where the distribution distances are computed based on features extracted from



Figure 4. Qualitative results for talking-head video synthesis on DFDC dataset.

the pre-trained InceptionV3 network. For video reconstruction tasks, the distance is measured with respect to the driving images, while for image animation tasks, it is measured with respect to the source.

- Semantic consistency – AKD (Average Key-point Distance): measures the average distance between key-points detected from the generated and real images. Following [37], for human body datasets, we use a pre-trained key-point detector by Cao et al. [5]; for human face datasets, we use the facial landmark detector by Bulat et al. [3].
- Animation identity preservation (for image animation) – CSIM: evaluates the quality of identity preservation. Specifically, it measures the cosine similarity between identity embedding vectors of the generated and real images. For human face datasets, the embeddings are extracted from a pre-trained face identity recognition model [8, 15, 44]. For human body datasets, we use the identity embeddings from the pre-trained Pytorch ReID model [37, 53]. CSIM is designed for animation tasks specifically, so the distance is measured with respect to the source.

4.1. Experimental Results

We train our model following the strategy of [37, 38], and re-train the baseline models [37, 38] with the same strategy. Throughout all experiments, we randomly select 3 reference images of the source object for our model. Same reference images are also used for image generation in all baseline models (one-shot) for fair comparisons, where the generated images with the best scores (L1 for reconstruction, FID for animation) are reported (results in parentheses of Tab. 1). Since there is no publicly available codes for Wang

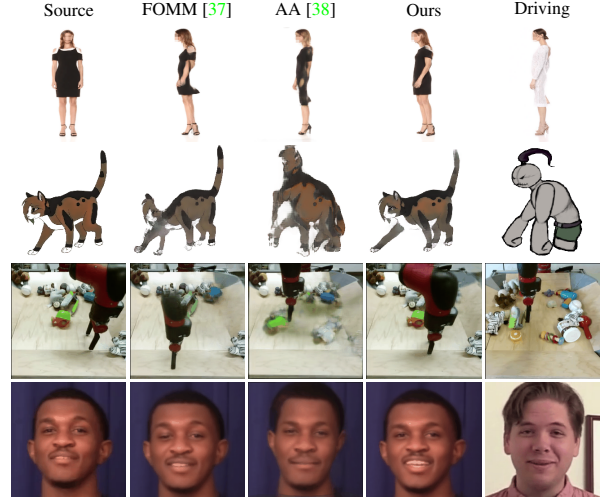


Figure 5. Qualitative results for image animation on Fashion (1st row), MGif (2nd row), Bair (3rd row) and DFDC (4th row).

et al. [44], we report their results on VoxCeleb listed in the original paper for reference.

Video Reconstruction We first compare our method with the state-of-the-arts for video reconstruction. Quantitative results are listed in Tab. 1 (note that face-vid2vid [44] is not applicable to datasets with objects other than talking heads). Clearly, our approach performs the best regarding every metric across all eight datasets, containing human faces, bodies, robots and cartoon animals. Notably, for the straightforward L1 reconstruction error, our approach outperforms all state-of-the-art methods by nearly 40% averagely. Using LPIPS, which was shown to correlate better with human observations [51], our approach improves the state-of-the-art by approximately 40% across all datasets. This could be also demonstrated by the qualitative comparisons for DFDC dataset shown in Fig. 4.

Image Animation We also report both quantitative (Tab. 1) and qualitative comparisons (Fig. 5) for the image animation task. For each dataset, we randomly generated 200 pairs of videos containing difference identities as source-driving pairs. On all eight datasets, our approach outperforms the state-of-the-art. Particularly, our approach achieves clear improvements in CSIM, which reflects how well the identity is preserved in the generated video compared to the source image. This result could be observed qualitatively in Fig. 5. In fact, we could observe that both FOMM [37] and AA [38] find it difficult to transfer the motion in the driving frame, which causes clear identity changes in the generated images. In contrast, our approach is able to transfer the motion better while preserving the source identity well.

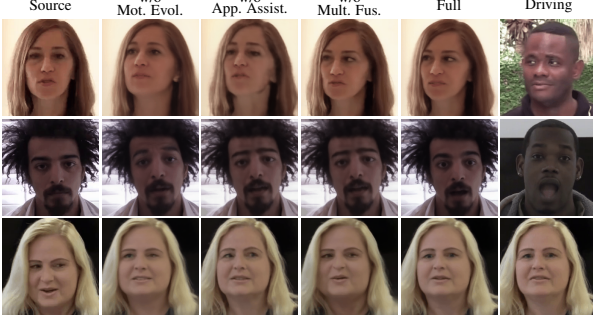


Figure 6. Ablation comparisons for talking-head animation on DFDC dataset.

Model Generality We further explore the model generality of all approaches. Specifically, we are interested in how all the various approaches compare, when trained on one specific dataset but tested on a different dataset (Fig. 2). We show the reconstruction results for models that were trained on VoxCeleb (face) dataset, but tested on Nemo (face) dataset, MGif (cartoons) dataset (Tab. 2). As demonstrated in Tab. 2, our approach achieves significant improvements across all metrics. Note that when tested on Nemo dataset, our model trained on VoxCeleb dataset even outperforms the state-of-the-art models originally trained on Nemo dataset (see Tab. 1). As illustrated in Fig. 2, when tested on domains different from VoxCeleb (human face dataset), both FOMM [37] and AA [38] struggle to preserve the source identities of cartoon animals.

Dataset	Method	L1 (↓)	LPIPS (↓)	FID (↓)	MS-/SSIM (↑)	PSNR (↑)	AKD (↓)
Nemo (124)	FOMM [37]	0.0191	0.047	37.57	0.94/0.91	29.93	1.36
	AA [38]	0.0170	0.045	33.95	0.95/0.92	30.38	1.24
	Ours (0)	0.0159	0.044	36.47	0.96/0.93	31.08	1.24
	Ours	0.0086	0.023	29.45	0.99/0.97	36.80	0.98
MGif (100)	FOMM [37]	0.086	0.256	222.99	0.76/0.63	15.38	N/A
	AA [38]	0.102	0.345	269.44	0.57/0.73	14.82	N/A
	Ours	0.045	0.176	158.96	0.81/0.86	18.70	N/A

Table 2. Model generality results for FOMM [37], Articulated Animation (AA) [38] and our approach. Results computed based on models trained on VoxCeleb dataset, while tested on Nemo (face) and MGif (cartoons) datasets.

4.2. Ablation Study

Model	Reconstruction						Animation	
	L1 (↓)	LPIPS (↓)	FID (↓)	MS-/SSIM (↑)	PSNR (↑)	AKD (↓)	FID (↓)	CSIM (↑)
Full	0.018	0.0061	33.22	0.95/0.91	27.99	1.28	64.89	0.92
w/o Mot. Evol.	0.022	0.082	42.47	0.93/0.87	28.60	1.53	71.88	0.88
w/o App. Assist.	0.024	0.085	41.89	0.92/0.85	27.88	1.29	75.35	0.90
w/o Mult. Fus.	0.032	0.108	54.57	0.88/0.84	24.24	1.78	80.34	0.89

Table 3. Ablations results of the proposed framework on DFDC dataset (1807 testing samples for reconstruction task, 200 testing pairs for animation), with mean results reported and best ones bolded. ↓ (↑) denotes that lower (higher) is better.

N	Reconstruction						Animation	
	L1 (↓)	LPIPS (↓)	FID (↓)	MS-/SSIM (↑)	PSNR (↑)	AKD (↓)	FID (↓)	CSIM (↑)
1	0.024	0.088	42.20	0.90/0.87	27.23	1.33	68.78	0.89
2	0.021	0.070	35.34	0.93/0.89	27.35	1.34	67.58	0.90
3*	0.018	0.0061	33.22	0.95/0.91	27.99	1.28	64.89	0.92
4	0.017	0.058	31.89	0.95/0.92	28.56	1.24	64.82	0.92
5	0.017	0.051	30.69	0.96/0.92	28.83	1.21	65.15	0.92
6	0.016	0.050	31.17	0.96/0.92	29.04	1.19	64.86	0.92

(*: equals to the full model used in this paper)

Table 4. Reconstruction & animation results for different choices of additional source view numbers (N), tested on DFDC dataset (1807 testing samples for reconstruction task, 200 testing pairs for animation), with mean results reported and best ones bolded. ↓ (↑) denotes that lower (higher) is better.

In order to analyze how each component (Sec. 3) in the proposed framework contributes to the final performance, we compare the following variants with our full model (with three input source views): (1) full model without motion evolution; (2) full model without self-appearance assistance; (3) model with only one input source view (w/o multi-view feature fusion from reference images). See detailed results in Tab. 3 and Fig. 6.

We also explore the model’s performance when varying the number of reference images used during testing. As indicated in Tab. 4, for the reconstruction task, increasing the number of reference images generally helps improve the model’s performance. On the other hand, for the animation task, increasing the number of reference images, which lead to higher memory cost, did not necessarily boost performance. Based on our experiments, three reference images could achieve reasonably good performance for both the reconstruction and animation tasks.

5. Conclusions

We proposed a general motion transfer framework for video reconstruction and image animation that is designed to handle large motion changes. Differentially refined using neural-ODEs, our approach obtains a dense motion deformation field as opposed to sparse key-points displacements. Equipped with the self-appearance flow, our approach utilizes the source features from different regions to help with inpainting occluded regions. Leveraging multiple reference images, our approach integrates the features from different viewpoints of the source object, and better preserves the source identity during image generation. Extensive experiments across eight datasets with objects varying from human faces, human bodies, robots and cartoon animals, demonstrate that the proposed framework consistently outperforms the state-of-the-art works by a large margin. Model generality analysis further shows that our approach performs well and stably even when tested across different object categories.

References

- [1] Bharat Lal Bhatnagar, Garvita Tiwari, Christian Theobalt, and Gerard Pons-Moll. Multi-garment net: Learning to dress 3d people from images. In *IEEE International Conference on Computer Vision (ICCV)*, 2019. 2
- [2] Volker Blanz and Thomas Vetter. A morphable model for the synthesis of 3d faces. In *Annual Conference on Computer Graphics and Interactive Techniques*, 1999. 1, 2
- [3] Adrian Bulat and Georgios Tzimiropoulos. How far are we from solving the 2d & 3d face alignment problem? (and a dataset of 230,000 3d facial landmarks). In *International Conference on Computer Vision (ICCV)*, 2017. 7
- [4] Chen Cao, Qiming Hou, and Kun Zhou. Displaced dynamic expression regression for real-time facial tracking and animation. *ACM Trans. Graph.*, 2014. 1, 2
- [5] Zhe Cao, Tomas Simon, Shih-En Wei, and Yaser Sheikh. Realtime multi-person 2d pose estimation using part affinity fields. In *IEEE/CVF Conference on Computer Vision and Pattern Recognition (CVPR)*, 2017. 1, 7
- [6] Caroline Chan, Shiry Ginosar, Tinghui Zhou, and Alexei A Efros. Everybody dance now. In *IEEE International Conference on Computer Vision (ICCV)*, 2019. 1
- [7] Ricky T. Q. Chen, Yulia Rubanova, Jesse Bettencourt, and David Duvenaud. Neural ordinary differential equations. In *Advances in Neural Information Processing Systems (NeurIPS)*, 2018. 3, 4
- [8] Jiankang Deng, Jia Guo, Xue Niannan, and Stefanos Zafeiriou. ArcFace: Additive angular margin loss for deep face recognition. In *IEEE/CVF Conference on Computer Vision and Pattern Recognition (CVPR)*, 2019. 7
- [9] Hamdi Dibeklioglu, Albert Ali Salah, and Theo Gevers. Are you really smiling at me? spontaneous versus posed enjoyment smiles. In *European Conference on Computer Vision (ECCV)*, 2012. 5
- [10] Hamdi Dibeklioglu, Albert Ali Salah, and Theo Gevers. Recognition of genuine smiles. *IEEE Transactions on Multimedia*, 17(3):279–294, 2015. 5
- [11] Brian Dolhansky, Joanna Bitton, Ben Pfau, Jikuo Lu, Russ Howes, Menglin Wang, and Cristian Canton Ferrer. The deepfake detection challenge dataset. *arXiv Preprint*, 2020. 5
- [12] Frederik Ebert, Chelsea Finn, Alex X. Lee, and Sergey Levine. Self-supervised visual planning with temporal skip connections. In *Conference on Robot Learning (CoRL)*, 2017. 6
- [13] Zhenglin Geng, Chen Cao, and Sergey Tulyakov. 3d guided fine-grained face manipulation. In *IEEE/CVF Conference on Computer Vision and Pattern Recognition (CVPR)*, 2019. 1, 2
- [14] Clément Godard, Oisín Mac Aodha, and Gabriel J. Brostow. Unsupervised monocular depth estimation with left-right consistency. In *IEEE/CVF Conference on Computer Vision and Pattern Recognition (CVPR)*, 2017. 3
- [15] Sungjoo Ha, Martin Kersner, Beomsu Kim, Seokjun Seo, and Dongyoung Kim. MarioNETte: Few-shot face reenactment preserving identity of unseen targets. In *Proceedings of the AAAI Conference on Artificial Intelligence (AAAI)*, 2020. 2, 7
- [16] Xiangyu He, Zitao Mo, Peisong Wang, Yang Liu, Mingyuan Yang, and Jian Cheng. Ode-inspired network design for single image super-resolution. In *IEEE/CVF Conference on Computer Vision and Pattern Recognition (CVPR)*, 2019. 3
- [17] Tomas Jakab, Ankush Gupta, Hakan Bilen, and Andrea Vedaldi. Unsupervised learning of object landmarks through conditional image generation. In *Advances in Neural Information Processing Systems (NeurIPS)*, 2018. 5
- [18] Justin Johnson, Alexandre Alahi, and Li Fei-Fei. Perceptual losses for real-time style transfer and super-resolution. In *European Conference of Computer vision (ECCV)*, 2016. 5
- [19] Jessica Lee, Deva Ramanan, and Rohit Girdhar. MetaPix: Few-Shot Video Retargeting. *ICLR*, 2020. 2
- [20] Yining Li, Chen Huang, and Chen Change Loy. Dense intrinsic appearance flow for human pose transfer. In *IEEE/CVF Conference on Computer Vision and Pattern Recognition (CVPR)*, 2019. 2
- [21] Peirong Liu, Lin Tian, Yubo Zhang, Stephen Aylward, Yueh Lee, and Marc Niethammer. Discovering hidden physics behind transport dynamics. In *IEEE/CVF Conference on Computer Vision and Pattern Recognition (CVPR)*, 2021. 3
- [22] Wen Liu, Zhixin Piao, Min Jie, Wenhan Luo, Lin Ma, and Shenghua Gao. Liquid warping gan: A unified framework for human motion imitation, appearance transfer and novel view synthesis. In *IEEE International Conference on Computer Vision (ICCV)*, 2019. 2
- [23] Matthew Loper, Naureen Mahmood, Javier Romero, Gerard Pons-Moll, and Michael J. Black. SMPL: A skinned multi-person linear model. *ACM Trans. Graphics (Proc. SIGGRAPH Asia)*, 2015. 2
- [24] Yiping Lu, Aoxiao Zhong, Quanzheng Li, and Bin Dong. Beyond finite layer neural networks: Bridging deep architectures and numerical differential equations. In *International Conference on Machine Learning (ICML)*, 2018. 3
- [25] Qianli Ma, Jinlong Yang, Anurag Ranjan, Sergi Pujades, Gerard Pons-Moll, Siyu Tang, and Michael J. Black. Learning to dress 3d people in generative clothing. In *IEEE/CVF Conference on Computer Vision and Pattern Recognition (CVPR)*, 2020. 2
- [26] Aymen Mir, Thimo Alldieck, and Gerard Pons-Moll. Learning to transfer texture from clothing images to 3d humans. In *IEEE/CVF Conference on Computer Vision and Pattern Recognition (CVPR)*. IEEE, 2020. 2
- [27] A. Nagrani, J. S. Chung, and A. Zisserman. Voxceleb: a large-scale speaker identification dataset. In *INTER-SPEECH*, 2017. 5, 6
- [28] Maxime Oquab, Pierre Stock, Oran Gafni, Daniel Haziza, Tao Xu, Peizhao Zhang, Onur Celebi, Yana Hasson, Patrick Labatut, Bobo Bose-Kolanu, Thibault Peyronel, and Camille Couprie. Low bandwidth video-chat compression using deep generative models. *arXiv Preprint*, 2020. 1
- [29] Mercedes E. Paoletti, Juan Mario Haut, Javier Plaza, and Antonio Plaza. Neural ordinary differential equations for hyperspectral image classification. *IEEE Transactions on Geoscience and Remote Sensing*, 2020. 3

- [30] Chaitanya Patel, Zhouyingcheng Liao, and Gerard Pons-Moll. Tailornet: Predicting clothing in 3d as a function of human pose, shape and garment style. In *IEEE/CVF Conference on Computer Vision and Pattern Recognition (CVPR)*. IEEE, 2020. 2
- [31] Shengju Qian, Kwan-Yee Lin, Wayne Wu, Yangxiaokang Liu, Quan Wang, Fumin Shen, Chen Qian, and Ran He. Make a face: Towards arbitrary high fidelity face manipulation. In *2019 IEEE/CVF International Conference on Computer Vision, ICCV*, 2019. 1, 2
- [32] Jian Ren, Menglei Chai, Oliver J. Woodford, Kyle Olszewski, and Sergey Tulyakov. Flow guided transformable bottleneck networks for motion retargeting. In *IEEE/CVF Conference on Computer Vision and Pattern Recognition (CVPR)*, 2021. 1, 2
- [33] Yurui Ren, Xiaoming Yu, Ruonan Zhang, Thomas H. Li, Shan Liu, and Ge Li. Structureflow: Image inpainting via structure-aware appearance flow. In *IEEE International Conference on Computer Vision (ICCV)*, 2019. 3, 4
- [34] Lars Ruthotto and Eldad Haber. Deep neural networks motivated by partial differential equations. *Journal of Mathematical Imaging and Vision*, 2018. 3
- [35] Maximilian Seitzer. pytorch-fid: FID Score for PyTorch. <https://github.com/mseitzer/pytorch-fid>, August 2020. Version 0.1.1. 6
- [36] Aliaksandr Siarohin, Stéphane Lathuilière, Sergey Tulyakov, Elisa Ricci, and Nicu Sebe. Animating arbitrary objects via deep motion transfer. In *IEEE/CVF Conference on Computer Vision and Pattern Recognition (CVPR)*, 2019. 2, 3, 4, 6
- [37] Aliaksandr Siarohin, Stéphane Lathuilière, Sergey Tulyakov, Elisa Ricci, and Nicu Sebe. First order motion model for image animation. In *Conference on Neural Information Processing Systems (NeurIPS)*, 2019. 2, 3, 4, 5, 6, 7, 8
- [38] Aliaksandr Siarohin, Oliver Woodford, Jian Ren, Menglei Chai, and Sergey Tulyakov. Motion representations for articulated animation. In *IEEE/CVF Conference on Computer Vision and Pattern Recognition (CVPR)*, 2021. 2, 3, 4, 5, 6, 7, 8
- [39] J. Thies, M. Zollhöfer, M. Stamminger, C. Theobalt, and M. Nießner. Face2Face: Real-time Face Capture and Reenactment of RGB Videos. In *IEEE/CVF Conference on Computer Vision and Pattern Recognition (CVPR)*, 2016. 1, 2
- [40] Shuhei Tsuchida, Satoru Fukayama, Masahiro Hamasaki, and Masataka Goto. AIST dance video database: Multi-genre, multi-dancer, and multi-camera database for dance information processing. In *International Society for Music Information Retrieval Conference (ISMIR)*, 2019. 5
- [41] Rafael Valle, Fitsum Reda, Mohammad Shoyebi, Patrick Legresley, Andrew Tao, and Bryan Catanzaro. Neural odes for image segmentation with level sets. *arXiv Preprint*, 2019. 3, 4
- [42] Ting-Chun Wang, Ming-Yu Liu, Andrew Tao, Guilin Liu, Jan Kautz, and Bryan Catanzaro. Few-shot video-to-video synthesis. In *Advances in Neural Information Processing Systems (NeurIPS)*, 2019. 2
- [43] Ting-Chun Wang, Ming-Yu Liu, Jun-Yan Zhu, Guilin Liu, Andrew Tao, Jan Kautz, and Bryan Catanzaro. Video-to-video synthesis. In *Advances in Neural Information Processing Systems (NeurIPS)*, 2018. 1, 2
- [44] Ting-Chun Wang, Arun Mallya, and Ming-Yu Liu. One-shot free-view neural talking-head synthesis for video conferencing. In *IEEE/CVF Conference on Computer Vision and Pattern Recognition (CVPR)*, 2021. 1, 2, 3, 4, 5, 6, 7
- [45] W. Wang, X. Alameda-Pineda, D. Xu, P. Fua, E. Ricci, and N. Sebe. Every smile is unique: Landmark-guided diverse smile generation. In *IEEE/CVF Conference on Computer Vision and Pattern Recognition (CVPR)*, 2018. 5
- [46] Olivia Wiles, A. Sophia Koepke, and Andrew Zisserman. X2face: A network for controlling face generation using images, audio, and pose codes. In Vittorio Ferrari, Martial Hebert, Cristian Sminchisescu, and Yair Weiss, editors, *European Conference on Computer Vision (ECCV)*, 2018. 2
- [47] Ali Pour Yazdanpanah and Simon K. Warfield Onur Afacan. Ode-based deep network for mri reconstruction. *arXiv Preprint*, 2019. 3
- [48] Polina Zablotskaia, Aliaksandr Siarohin, Bo Zhao, and Leonid Sigal. Dwnet: Dense warp-based network for pose-guided human video generation. In *British Machine Vision Conference (BMVC)*, 2019. 6
- [49] Egor Zakharov, Aleksei Ivakhnenko, Aliaksandra Shysheya, and Victor Lempitsky. Fast bi-layer neural synthesis of one-shot realistic head avatars. In *European Conference of Computer vision (ECCV)*, 2020. 1, 2
- [50] Egor Zakharov, Aliaksandra Shysheya, Egor Burkov, and Victor Lempitsky. Few-shot adversarial learning of realistic neural talking head models. In *IEEE/CVF Conference on Computer Vision and Pattern Recognition (CVPR)*, 2019. 1, 2
- [51] Richard Zhang, Phillip Isola, Alexei A Efros, Eli Shechtman, and Oliver Wang. The unreasonable effectiveness of deep features as a perceptual metric. In *IEEE/CVF Conference on Computer Vision and Pattern Recognition (CVPR)*, 2018. 6, 7
- [52] Tianjun Zhang, Zhewei Yao, Amir Gholami, Joseph E Gonzalez, Kurt Keutzer, Michael W Mahoney, and George Biros. Anodev2: A coupled neural ode framework. In H. Wallach, H. Larochelle, A. Beygelzimer, F. d'Alché-Buc, E. Fox, and R. Garnett, editors, *Advances in Neural Information Processing Systems (NeurIPS)*, 2019. 3, 4
- [53] Zhedong Zheng, Xiaodong Yang, Zhiding Yu, Liang Zheng, Yi Yang, and Jan Kautz. Joint discriminative and generative learning for person re-identification. In *IEEE/CVF Conference on Computer Vision and Pattern Recognition (CVPR)*, 2019. 7
- [54] Tinghui Zhou, Shubham Tulsiani, Weilun Sun, Jitendra Malik, and Alexei A Efros. View synthesis by appearance flow. In *European Conference on Computer Vision (ECCV)*, 2016. 3, 4
- [55] M. Zollhöfer, J. Thies, P. Garrido, D. Bradley, T. Beeler, P. Pérez, M. Stamminger, M. Nießner, and C. Theobalt. State of the art on monocular 3d face reconstruction, tracking, and applications. *Computer Graphics Forum*, 2018. 1, 2